Uranium redox transition pathways in acetate-amended sediments

John R. Bargar[a,1], Kenneth H. Williams[b], Kate M. Campbell[c], Philip E. Long[b], Joanne E. Stubbs[a,2], Elenal I. Suvorova[d], Juan S. Lezama-Pacheco[a,3], Daniel S. Alessi[d], Malgorzata Stylo[d], Samuel M. Webb[a], James A. Davis[b], Daniel E. Giammar[e], Lisa Y. Blue[e,4], and Rizlan Bernier-Latmani[d]

[a]Chemistry and Catalysis Division, Stanford Synchrotron Radiation Lightsource, SLAC National Accelerator Laboratory, Menlo Park, CA 94025; [b]Earth Sciences Division, Lawrence Berkeley National Laboratory, Berkeley, CA 94720; [c]US Geological Survey, Boulder, CO 80303; [d]Environmental Microbiology Laboratory, Ecole Polytechnique Fédérale de Lausanne, CH-1015 Lausanne, Switzerland; and [e]Department of Energy, Environmental and Chemical Engineering, Washington University, Saint Louis, MO 63130

Edited by Thure E. Cerling, University of Utah, Salt Lake City, UT, and approved February 6, 2013 (received for review November 6, 2012)

Redox transitions of uranium [from U(VI) to U(IV)] in low-temperature sediments govern the mobility of uranium in the environment and the accumulation of uranium in ore bodies, and inform our understanding of Earth's geochemical history. The molecular-scale mechanistic pathways of these transitions determine the U(IV) products formed, thus influencing uranium isotope fractionation, reoxidation, and transport in sediments. Studies that improve our understanding of these pathways have the potential to substantially advance process understanding across a number of earth sciences disciplines. Detailed mechanistic information regarding uranium redox transitions in field sediments is largely nonexistent, owing to the difficulty of directly observing molecular-scale processes in the subsurface and the compositional/physical complexity of subsurface systems. Here, we present results from an in situ study of uranium redox transitions occurring in aquifer sediments under sulfate-reducing conditions. Based on molecular-scale spectroscopic, pore-scale geochemical, and macroscale aqueous evidence, we propose a biotic–abiotic transition pathway in which biomass-hosted mackinawite (FeS) is an electron source to reduce U(VI) to U(IV), which subsequently reacts with biomass to produce monomeric U(IV) species. A species resembling nanoscale uraninite is also present, implying the operation of at least two redox transition pathways. The presence of multiple pathways in low-temperature sediments unifies apparently contrasting prior observations and helps to explain sustained uranium reduction under disparate biogeochemical conditions. These findings have direct implications for our understanding of uranium bioremediation, ore formation, and global geochemical processes.

metal reduction | roll front | sulfate reduction | sulfide | bioreduction

Uranium redox transitions [from U(VI) to U(IV)] in low-temperature sediments control the mobility of uranium in suboxic and reduced aquifers (1), mediate uranium accumulation in ores (2), and govern $^{238}U/^{235}U$ fractionation in seawater, of interest as a paleo-redox proxy (3, 4). Distinguishing the nature of the reaction pathway responsible for reducing U(VI) in field sediments remains a central challenge to advancing mechanistic understanding of these important transitions. The inaccessibility of the subsurface and the dilute concentrations of uranium in natural sediments, typically <1 mg/kg, have effectively prevented direct observation of pathways at the critical molecular to grain scales at which these reactions occur. Important parameters for which information is needed in bona fide field sediments include the number of reduction pathways operating, the reactants, especially the electron donor, and the products. In the absence of such information, biogeochemical models have invoked simplified pathways (5, 6), typically involving a single type of reducing agent and assuming uraninite (UO_2) as the U(IV) product. Recent laboratory studies report that bioreduced U(IV) occurs as uraninite and less stable (7) monomeric forms of U(IV) coordinated to phosphate or carbonate groups on biological surfaces or in amorphous or nanocrystalline precipitates (8–14). Monomeric U(IV) also has been reported in reduced field sediments (15, 16). The presence of less stable forms of U(IV) raises important questions for uranium biogeochemistry and uranium redox transition pathways in natural sediments. However, no study has linked U(IV) molecular structure to pore-scale sediment geochemistry to deduce reduction pathways.

Both biological and abiotic reducing agents are available in sediments and coexist at the scale of sediment pores and grain coatings (nanometers to tens of micrometers). Sulfate-reducing bacteria (SRB) are important in the mineralization of FeS_2 in low-temperature sandstone-type ores, sustained by transfer of electrons from organic carbon [hydrocarbons (17–20), plant materials (21, 22), or their fermentative products] to sulfate (17, 21). SRB along with metal-reducing bacteria (MRB) (23, 24) also are capable of enzymatically reducing U(VI) to U(IV). Indeed, indirect evidence suggests that enzymatic pathways dominate under conditions of subsurface biostimulation, particularly under conditions dominated by MRB (5, 6, 25–27). Moreover, recent evidence from genomic (28) and petrologic (18, 19) studies suggests that direct enzymatic reduction of U(VI) contributes to the mineralization of U(IV) in low-temperature sandstone-type uranium ores. Abiotic reducing agents in ore deposits, shallow contaminated aquifers, and marine sediments include pyrite, aqueous bisulfide (22, 29–33), mackinawite (FeS) (34), magnetite (Fe_3O_4) (35–37), green rust (38), Fe^{2+} adsorbed on Fe oxides (39), and structural Fe^{2+} in clays (40). The presence of so many potential reducing agents makes it difficult to deduce the nature of redox transition pathways. Studies that link molecular-scale U(IV) speciation to pore-scale mineralogy and macroscale behavior over defined time intervals are needed to better understand redox transition mechanisms and the biogeochemical processes they control.

In the present study, we have connected uranium speciation, sediment geochemistry, and time to obtain unprecedented

Author contributions: J.R.B., K.M.C., P.E.L., J.A.D., and R.B.-L. designed research; J.R.B., K.H.W., J.E.S., E.I.S., J.S.L.-P., D.S.A., M.S., S.M.W., D.E.G., L.Y.B., and R.B.-L. performed research; J.R.B., K.H.W., K.M.C., P.E.L., and J.A.D. contributed new reagents/analytic tools; J.R.B., J.E.S., E.I.S., J.S.L.-P., D.S.A., M.S., and S.M.W. analyzed data; and J.R.B. wrote the paper.

The authors declare no conflict of interest.

This article is a PNAS Direct Submission.

Freely available online through the PNAS open access option.

[1]To whom correspondence should be addressed. E-mail: bargar@slac.stanford.edu.

[2]Present address: Center for Advanced Radiation Sources, University of Chicago, Chicago, IL 60637.

[3]Department of Environmental Earth System Science, Stanford University, Stanford, CA 94305.

[4]Present address: Covalent Research Technologies, LLC, Lexington, KY 40507.

This article contains supporting information online at www.pnas.org/lookup/suppl/doi:10.1073/pnas.1219198110/-/DCSupplemental.

molecular- to pore-scale information about biogeochemical pathways leading to the formation of specific U(IV) species in field sediments under sulfate-reducing conditions. To obtain such information over a defined time interval, we deployed in situ sediment reactors in wells in the alluvial aquifer at Rifle, Colorado, during acetate amendment of the aquifer. This approach hydrologically and biogeochemically connects the sediments to groundwater and enables easy retrieval for subsequent analysis. Harvested sediments were characterized by X-ray and electron microscopy, synchrotron-based X-ray absorption spectroscopy, and bulk extraction and digestion techniques. These measurements show that U(VI) was reduced to monomeric U(IV) species (complexes or nanoscale precipitates) likely associated with biomass and to an ordered species resembling uraninite. The presence of multiple products suggests multiple redox transition pathways were operational. The reduction of U(VI) by mackinawite (FeS), coupled to binding of U(IV) by biopolymers, is proposed. The presence of multiple redox transition pathways unifies previous observations and has important implications for uranium biogeochemistry in reduced sediments.

Results

In situ reactors containing fresh field sediments were installed into neighboring wells P-101 and P-102 at the Rifle Integrated Field Research Challenge (IFRC) site in Rifle, Colorado, before a field acetate amendment experiment (41). The wells exhibit similar groundwater composition and microbial ecology (27, 41). Comparing results from the two wells provides an estimate of the overall variability in the experiment. Groundwater was continuously eluted through the columns to hydrologically connect them to aquifer biogeochemical dynamics. Millimolar concentrations of acetate and ≤20 μM uranyl were added to column influents to obtain sediment uranium concentrations adequate for spectroscopic and microscopic analysis. Effluent and groundwater data (*SI Text* and Fig. S1) show that uranium reduction was minor during the initial, brief (~10 d) iron-reducing stage in the aquifer. The majority of U(IV) accumulated under subsequent sulfate-reducing conditions, obtaining concentrations ≤485 mg/kg (Table 1). Removal of U(VI) during sulfate reduction has been demonstrated in laboratory column studies (42). The present study demonstrates this behavior in an aquifer and is consistent with biogeochemical results from multiple field-scale acetate amendment experiments (27).

Microbial Communities Present During in Situ Bioreduction. Sediment microbial communities were initially relatively diverse and included Proteobacteria such as the metal-reducing bacterium *Shewanella* spp. and the sulfate-reducing bacterium *Desulfobacter* spp. In addition, Firmicutes and Acidobacteria were also present in significant numbers (Fig. S2). After acetate amendment, in situ column sediment communities were dominated by SRB Desulfobacterales, confirming sulfate-reducing conditions. Additionally, Clostridiales, an order of primarily fermentative bacteria, increased in abundance, suggesting a role for fermenters in the breakdown of biomass. Among the phyla stimulated by acetate amendment, only Deltaproteobacteria and Firmicutes have members well known to be capable of enzymatic U(VI) reduction.

Microscale/Nanoscale Distribution of Uranium, Iron, and Sulfur in Bioreduced Sediments. X-ray microprobe (XRM), scanning electron microscopy (SEM), and transmission electron microscopy (TEM) analyses were used to characterize column sediments. XRM measurements show that preamendment sediments exhibited Fe-rich coatings devoid of detectable U. SEM shows them to be of submicrometer dimension and containing clays and Fe oxides but not S (Fig. S3). After the experiment, sediment grains exhibited extensive Fe-rich coatings and mineralized cracks, in some cases exceeding 10-μm thicknesses (Fig. 1). X-ray energy-dispersive spectra (EDS) showed good to excellent correlation of Fe and S atomic percentages, implying the presence of a ferrous sulfide or bisulfide phase. This correlation was observed in 12 of 18 coatings examined with SEM (Table S1 and Figs. S4–S6). Selected area electron diffraction (SAED) showed mackinawite (FeS) to be abundant in the coatings (Figs. S5 and S6). FeS_2, not observed in TEM measurements, is not expected given its sluggish formation kinetics (43). The other six coatings exhibited poor Fe:S correlations. These coatings contained Fe and O at higher abundances than S, and contained little or no detectable Si and Al, indicating that FeS and/or Fe-rich clays were minor. Fe oxide phases likely were the most abundant at these locations. These observations are illustrated in Fig. 2, which shows the presence of two dominant Fe species around a single grain. Micro–X-ray absorption near-edge structure (μ-XANES) spectra from the sulfidic portions resemble mackinawite, consistent with electron microscopy results. XANES from the oxide region resemble ferrihydrite, a poorly crystalline ferric oxy-hydroxide that also serves as a proxy for goethite and hematite and indicates the presence of Fe^{3+}. HS^-(aq) produced during sulfate reduction (27) chemically reduces Fe(III) oxides, producing S^0 and Fe^{2+} (5, 27, 44). The latter reacts with HS^-(aq) to precipitate mackinawite. The coassociation of FeS with Fe(III) oxides in the coatings is therefore consistent with sulfate-reducing conditions, and implies that S^0 is present. Indeed, S:Fe ratios >1, common in the sulfidic coatings (Table S1 and Figs. S4–S6), are consistent with excess S being present as S^0.

At the scale of whole-sediment clasts, U was associated with the sulfidic coatings and not with Fe oxides (Fig. 2). U is distributed throughout the coatings, indicating that U(IV) and mackinawite formed concurrently, consistent with sulfate-reducing conditions. An additional example of this behavior is provided in Fig. S7. The apparent correlation between U and FeS, however, does not hold up at micrometer and submicrometer scales. As shown in Fig. 1,

Table 1. Uranium extracted from sediment samples in milligrams of U per kilograms of dry sediment

Sample	1 M HCO_3 extraction, mg/kg	Aqua regia digestion, mg/kg	Total U concentration, mg/kg
P-101			
Preamendment	NA	0.8 (0.13)	0.8 (0.13)
Top	NA	229 (2)*	229 (2)*
Bot	NA	190 (12)	190 (12)
P-102			
Preamendment	NA	0.5 (0.10)	0.5 (0.10)
Top preaging	364 (25)*	121 (8)*	485 (33)*
Bot postaging	123 (8)*	131 (9)*	254 (17)*

"Top" and "bot" indicate effluent and influent ends of columns, respectively. Estimated SDs (ESDs) based on replicates and instrumental error are listed in parentheses. Total U is the sum of HCO_3 and aqua regia-extracted U (*SI Text*).
*ESDs for this data point are based on instrumental errors because a sufficient quantity of sediment was unavailable for replicates.

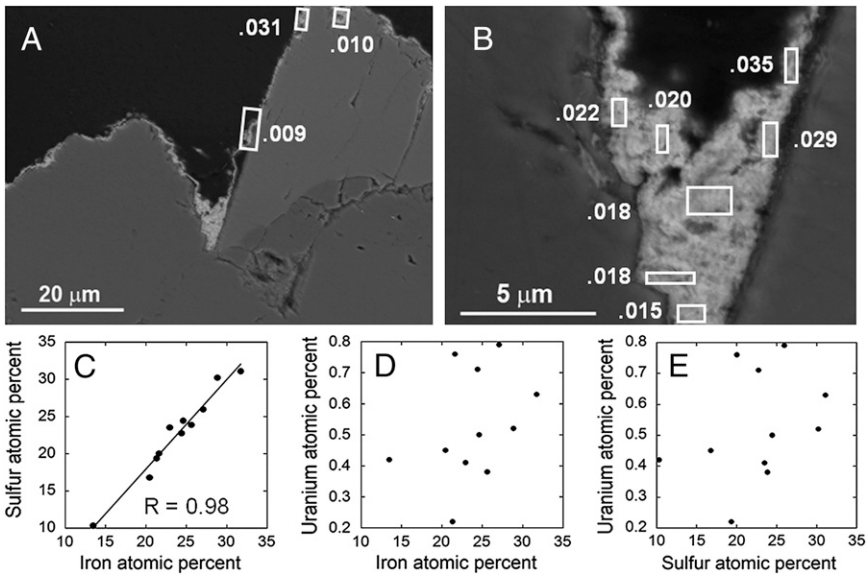

Fig. 1. Sulfidic coatings on grain "t10 p16a/b." (*A* and *B*) Backscattered electron micrographs. The image in *B* is a high-magnification detail of the central region in *A*. EDS analysis areas are as indicated in the white boxes. Values indicated on SEM image are EDS-derived atomic U:Fe ratios. (*C*–*E*) Scatter plots showing EDS-derived atomic percentages of U, Fe, and S. Data from additional grains are provided in Table S1 and Figs. S4–S6.

large variations in U:Fe ratios within small portions of individual coatings led to poor or no U:Fe correlations within coatings. This behavior was also observed in most of the other locations examined (Figs. S4–S6).

Bulk Spectroscopic Characterization and Chemical Extractions. U L_{II} XANES spectra show that the sediments predominantly have U(IV) (Fig. S8). Fourier transforms (FTs) of U L_{II} extended X-ray absorption fine structure (EXAFS) spectra (Fig. 3) show the presence of a U-O pair correlation at ~1.9 Å, indicating oxo-coordination of U(IV). [This value is phase-shifted by dR; the corresponding U-O interatomic distance (*D*) is ~2.35 Å.] All FTs also display a frequency at ~2.9 Å, which can be attributed to bidentate P ligands; it is at a different position than observed in biological U(IV)-carbonate precipitates (12). Frequencies at this position have been reported for biologically reduced U(VI) bound to P/C-containing groups associated with biomass (8–13). Coordination to phosphoryl and/or carboxyl functional groups on cells and extracellular polysaccharides (9) and precipitation of amorphous or nanocrystalline inorganic U(IV)-phosphates (9, 12) are plausible. Although U(IV) has been described as "monomeric" or "mononuclear" (i.e., implying coordination complexes)

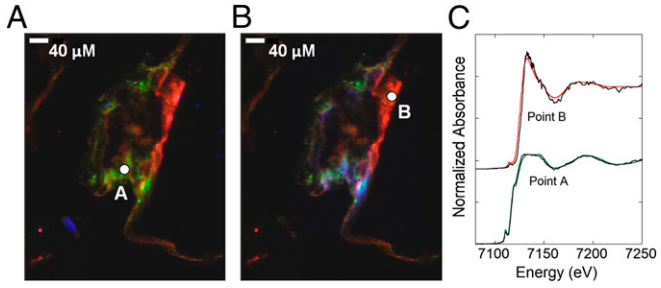

Fig. 2. (*A*) Tricolor XRM image grain "3_Jan2010" from P-101 displaying results of principal component analysis based on 58 separate K-edge μ-XANES spectra. Red shows locations where XANES are characteristic of Fe (III) oxides, green areas are characteristic of Fe(II) sulfides, and blue corresponds to Fe-bearing clays. (*B*) Same color scheme as *A*, except blue has been reassigned to show U fluorescence. Note that U is colocated with Fe sulfides. (*C*) Fe K-edge XANES spectra (black) from locations marked A and B in *A* and *B*. The red spectrum is ferrihydrite, and the green spectrum is a linear combination of 93% mackinawite and 7% ferrihydrite.

(8–13), phosphate also occurs as polymeric networks in U(IV)-phosphates. Consequently, U(IV) bound to phosphate polymers [i.e., U(IV) coordination polymers] also must be considered. U EXAFS cannot distinguish the degree of phosphate polymerization. For clarity, we explicitly define our use of "monomeric U(VI)" to include monomeric complexes and coordination polymers. SEM-EDS measurements show that P was present in the coatings at most locations where U was located (Table S1). The presence of P can be used as an indicator for biomass because the Old Rifle aquifer is deficient in dissolved phosphate and phosphate minerals (16, 45). Consequently, fits to the EXAFS were performed using U(IV)-P shells [or U(IV)-C shells] at interatomic distances observed in biomass (~3.15 and 3.6 Å) (9). These fits provide good reproductions of the spectra (Fig. 3, Fig. S8, and Table S2). Similar products were observed in sulfidic Old Rifle sediments reduced by natural organic carbon (16), suggesting that the present results are representative of native aquifer processes.

A third pair correlation at ~3.6 Å is present in the FTs. This feature can be fit with a shell of U atoms at ~3.8 Å and suggests the presence of polymerized U(IV) complexes or a phase such as uraninite (UO_2) or coffinite ($USiO_4$). U(IV) generally was not associated with silicate in the samples. However, uraninite is a plausible phase and frequently has been observed in laboratory U(VI) bioreduction experiments (7).

Bicarbonate extractions (7) were performed to quantify pools of recalcitrant (UO_2) and less stable (monomeric) forms of U(IV) (*SI Text*). As shown in Table 1, 75 ± 7% of U(IV) in the sediments was extractable at the end of the initial 90-d experiment. Uraninite is inferred to be present at lower but significant concentrations (i.e., 25 ± 2.4%). These results indicate that monomeric U(IV) was the dominant uranium species (7), corroborating the EXAFS-derived conclusions. After correcting for losses of monomeric U(IV) during the final flushing step of the subsequent 1-y in-well aging experiment, uraninite abundance is estimated at 26 ± 2.4% (*SI Text*). Thus, uraninite relative abundance did not significantly increase during a year of aging in the aquifer. These results do not support a monomeric U(IV) → uraninite transformation. The presence of two distinct U(IV) products implies that at least two redox transition pathways were operative during uranium reduction (12).

Discussion

The presence of multiple redox transition pathways allows for different U(IV) products to be formed under variable biogeochemical

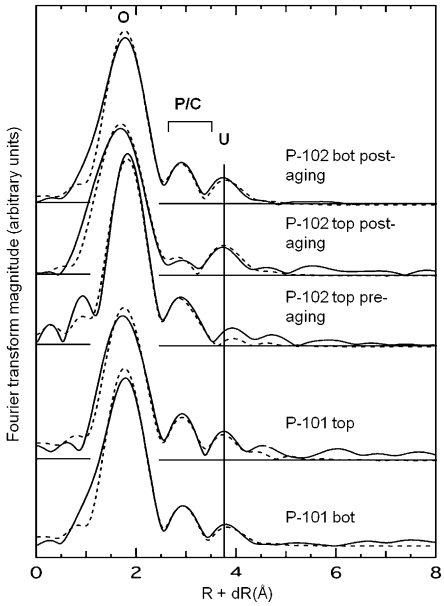

Fig. 3. Fourier transforms of U L_{II} EXAFS spectra (lines) from in situ columns. EXAFS data are provided in Fig. S8. The dashed lines are fits to spectra.

conditions. For example, monomeric U(IV) complexes were observed in ethanol-stimulated field sediments at the Oak Ridge, Tennessee, site (15), whereas the same sediments yielded UO_2 when reduction occurred in the laboratory (13, 15). The presence of multiple pathways also is consistent with reductive uranium immobilization under both iron- and sulfate-reducing conditions (42, 46).

Mackinawite Mineralization. Surface-associated sulfidic minerals occur as coatings that are contiguous for tens of micrometers around grains continuing into cracks that are deeply and completely filled with the coating material (e.g., Fig. 1 and Figs. S4 and S5), suggesting that the coatings formed in place and not from adventitious association of fine-grained materials during sample processing. MRB physiology changes from planktonic to surface-attached at the onset of sulfate reduction (26), and SRB also are expected to be surface-attached. Attachment is facilitated by the production of extracellular polymeric (organic) substances (EPS) (47) (Fig. 4), which provides abundant nucleation sites for kinetically facile precipitation of FeS (48, 49). HS^- and Fe^{2+} are present in groundwater and also are supplied locally by sulfate reduction and subsequent reaction of HS^- with Fe(III) oxides. Thus, development of extensive FeS coatings in the aquifer sediments can be explained via a mixed biotic–abiotic reaction sequence, involving attachment of biopolymers to mineral surfaces followed by precipitation of mackinawite. ^{32}S-enriched HS^- is produced by biological sulfate reduction (50). If incorporated into precipitating mackinawite and retained during transformation to FeS_2 (48), this reaction sequence could produce biological enrichment of ^{32}S in pyrite similar to that observed in uranium ores (17–21).

U(VI) Reduction Pathways Under Sulfate-Reducing Conditions. The apparent grain-scale spatial association between U(IV) and mackinawite implies that the mackinawite pool is of central importance to uranium redox transitions, likely as a reducing agent for U(VI). HS^-(aq) is expected to be insignificant as a reductant for U(VI) in Old Rifle groundwater (51). However, direct abiotic reduction of U(VI) by mackinawite (34), as well as by other ferrous sulfides and oxides (29, 30, 35–38), produces uraninite when dissolved phosphate is low or deficient, as is the case in Rifle groundwater (≤0.1 μM) (45). Thus, a simple reaction mechanism in which U(VI) is reduced on mackinawite surfaces can account for the presence of uraninite in the samples. However, it cannot explain the abundance of monomeric U(IV) species, nor the lack of correlation between U and Fe at the micrometer and submicrometer scales. An additional reaction step is needed to reconcile an "abiotic" redox pathway with these observations. Such a step can exist in the presence of biologically produced phosphate. Binding to phosphate groups in biomass, on mineral surfaces, or aqueous solution stabilizes monomeric U(IV) (as complexes or possibly amorphous/nanocrystalline precipitates) and suppresses uraninite formation (12, 37). The posited biomass and EPS enshrouding mackinawite (Fig. 4) would provide a source of high-affinity U(IV)-binding phosphate sites (52). Phosphate is also released from cell lysis and can precipitate with uranium (14, 53). The intimate association of biomass and mackinawite (Fig. 4) thus provides a mechanical juxtaposition of reactants capable of producing phosphate-U(IV) complexes, polymers, or solids. The latter pathway has not previously been proposed. If biomass were absent, we would expect uraninite precipitation (34). Enzymatic U(VI) reduction products include monomeric U(IV) (9–12) and uraninite (9, 54), both present in these samples. Consequently, U(VI) reduction by bacteria associated with mackinawite and not with Fe oxides also is consistent with our results. Because monomeric U(IV) and uraninite can be produced by multiple routes, it is not possible to definitively attribute specific products to specific pathways at this time.

Acetate amendment of the Old Rifle aquifer results in preferential accumulation of ^{238}U in reduced uranium products (55), also observed in sandstone-type uranium ore deposits and pelagic sediments (3, 4, 56). The present study associates this behavior with monomeric U(IV) species, raising the possibility of a molecular-scale link between these species and isotope fractionation processes.

Implications for Uranium Bioremediation and Reactive Transport Modeling. U(VI) concentrations in this study are consistent with contaminated Colorado River basin sites (<54 μM) (45). Throughout this region, aqueous uranium is dominated by uranyl-calcium-carbonate complexes. The present findings are thus regionally relevant.

The participation of sulfides in U(VI) reduction may help to explain sustained removal of U(VI) in biostimulated aquifers after cessation of acetate amendments (27). Moreover, the intimate dissemination of U(IV) within a matrix of iron sulfides provides physical and chemical barriers to reoxidation (57, 58). Counteracting these effects, the relative abundance of monomeric U(IV) suggests that a large pool of bioreduced uranium

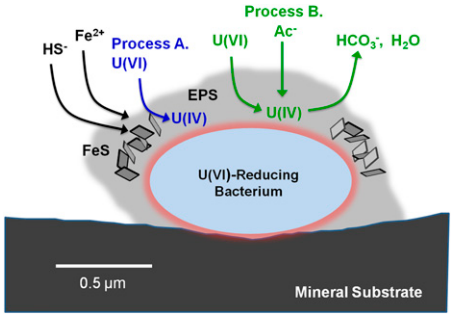

Fig. 4. Conceptual model for uranium bioreduction in sediments under sulfate-reducing conditions. FeS nucleates and grows at cell surfaces and throughout EPS matrix. Process A: U(VI) is reduced dominantly via a mixed abiotic–biotic pathway involving mackinawite (FeS) as an electron donor and biomass as a U(IV) binding agent. It is also likely that biological reduction of U(VI) (Process B) occurs concurrent with Process A.

may be susceptible to rapid mobilization if challenged by oxidants. Consequently, the behavior of U(IV) will depend on a complex interplay between chemical, hydrological, and physical conditions occurring in the matrix. These results underscore the need for reactive transport models that can describe the behavior of nonuraninite forms of U(IV) in biostimulated aquifers.

Implications for Uranium Ore Genesis. Several types of uranium deposits, including sandstone ores, exhibit abundant organic material (17–22, 59–63), sulfate/sulfide (17, 22), dissolved organic carbon (DOC) up to 50 mg/L (59), and uranium up to micromolar concentrations (59, 61, 64–66). Although acetate was the dominant DOC in the present investigation, monomeric U(IV) and uraninite are both produced in the presence of a wide variety of electron donors (7–9, 12, 14). U(IV) occurs as uraninite and coffinite in sandstone-type deposits (67). U(IV)-phosphates are reported in other ore types (68). Monomeric U(IV) species generally do not diffract X-rays, and their presence in ores may have been widely overlooked. More work is required to address the potential roles of these easily remobilized species (7) in ore genesis and in situ uranium recovery from subsurface deposits.

In comparison with ores, the higher U(VI) (5-20 μM) and DOC (75–300 mg/L) concentrations in this study are expected to facilitate somewhat faster biological and abiotic U(VI) reduction (6, 69). It is likely that rates of competing reduction pathways [e.g., precipitation of uraninite vs. monomeric U(IV)] differ in response to U(VI) and DOC concentrations, leading to variable U(IV) product assemblages. Further research is needed to understand the roles of dissolved uranium concentrations and biomass–mineral–uranium interactions as controls over U(VI) reduction rates and U(IV) products in ores.

Materials and Methods

Field Experiments. Fresh sediments were cored from the Rifle IFRC experimental plot C, sieved moist to <2 mm under N_2, packed into PVC columns (25 mm diameter, 150 mm long), and reinstalled into neighboring wells P-101 and P-102 in plot C on the same day to 5 m below ground surface (~1.5 m below the water table). Columns were eluted with groundwater (0.2 mL/min flow rate) for 6 d to recondition sediments in the aquifer. Coinciding with the start of a 3 mM acetate field amendment (41) on July 22, 2009, continuous additions of acetate and U(VI) in groundwater were introduced to influents to obtain concentrations of 5 mM and 20 μM, respectively. Acetate additions to the columns ensured that U(VI) reduction would occur even if the field acetate plume did not reach the experiment. On day 16, effluent flow rates were increased to 0.4 mL/min to obtain a more stable flow, resulting in reduced in-column acetate and U(VI) influent concentrations (2.5 mM and 10 μM). U(VI) amendment was halted between days 60 and 68 to assess elution of uranium during groundwater flushing. On day 83, influent acetate and uranium inflows were decreased to obtain 1.25 mM and 5 μM, respectively, to extend the life of the influent reservoir during a period of infrequent site visits. U amendment was ceased on day 90. Columns were flushed with groundwater for 9 d (P-101) and 4 d (P-102) to desorb U(VI) to minimize its interference in spectra and then removed from the wells. The P-102 column was subsampled at the effluent end, backfilled with clean borosilicate glass beads, and reinstalled to examine changes in U(IV) speciation after aging. After 385 d, it was flushed with groundwater (14 d) and harvested. Additional sample handling is described in *SI Text*.

Thin-Section Preparation. Sediments were dried and embedded in degassed epoxy (EpoTek 301) under 5% H_2/95% N_2. Petrographic thin sections were prepared (Spectrum Petrographics). XRM analyses were done in air, but thin sections were otherwise stored anaerobically.

Electron Microscopy. SEM and EDS were measured (INCA system) at 10 kV accelerating voltage (XL30F Sirion; FEI) from carbon-coated thin sections. TEM samples were prepared using a focused ion beam [Zeiss NVision 40 focused ion beam (FIB), Zeiss; and FEI Strata 235DB dual-beam FIB/SEM]. Bright/dark-field and scanning transmission electron microscopy (BF/DF TEM, STEM), high-resolution TEM, and SAED were performed at 300 kV (FEI CM300UT/FEG; FEI). Images and SAED patterns (Gatan 797 slow scan CCD camera and Digital Micrograph software; Gatan) were calculated using the Java Electron Microscopy Software (JEMS) (70).

16s rRNA Gene-Based Community Analysis. Sediment from wells and columns was stored at −80 °C until DNA was extracted (71), amplified, and sequenced as described in *SI Text*. Operational taxonomic units (OTUs) were defined by the UCLUST algorithm, based on a similarity threshold of 97% (72). OTUs were aligned with PyNAST, which works from a Greengenes template file containing prealigned 16S rRNA sequences (73). The phylogenetic assignment was carried out by the RDP classifier (74).

X-Ray Microscopy. The full petrographic thin sections were initially mapped at the Stanford Synchrotron Radiation Lightsource (SSRL) beam line 10-2 (25-μm spot). X-ray microprobe images and micro–X-ray absorption spectroscopy (μ-XAS) spectra were collected at beam line 2-3 (2-μm spot; Vortex fluorescence detector) at 17,200 eV, and 17,100 eV. Difference maps [MicroAnalysis Toolkit (75)] were calculated to isolate U Lα signal.

XAS. Fluorescence-yield uranium XAS spectra were measured at SSRL beam line 11-2 [77K, double-crystal Si(220) monochromator detuned 20%, 30-element germanium detector array]. Energy calibration was monitored using a Y foil. EXAFS data were extracted and fit (76, 77) using calculated phase and amplitude functions [FEFF8.4 (78)].

Chemical Extractions. Bicarbonate extractions were performed to assess the distribution of U(IV) between uraninite and more labile noncrystalline forms of U(IV) (7). Remaining U was subsequently extracted by digesting the remaining solids in aqua regia (*SI Text*).

ACKNOWLEDGMENTS. We thank Kate Maher, Ed Landa, and two anonymous reviewers for helpful discussions and comments. Work at SLAC (Work Package 10094), the Rifle Integrated Field Research Challenge, and Lawrence Berkeley National Laboratory were funded by the Department of Energy Office of Science (DOE-SC), Office of Biological and Environmental Research (BER). Additional support was provided by a US Geological Survey National Research Council Fellowship (to K.M.C.), Swiss National Science Foundation Grants 20021-113784 and 200020-126821 (to M.S. and D.S.A.), and Marie Curie Program Grant FP7-PEOPLE-2009-IIF-254143 (to D.S.A.). Stanford Synchrotron Radiation Lightsource (SSRL) is a DOE Office of Basic Energy Sciences User Facility operated by Stanford University. The SSRL Structural Molecular Biology Program is supported by DOE-SC-BER, and by the National Institutes of Health (NIH)–National Institute of General Medical Sciences (including Grant P41GM103393) and NIH–National Center for Research Resources (Grant P41RR001209).

1. Wall JD, Krumholz LR (2006) Uranium reduction. *Annu Rev Microbiol* 60:149–166.
2. Hobday DK, Galloway WE (1999) Groundwater processes acid sedimentary uranium deposits. *Hydrogeol J* 7(1):127–138.
3. Brennecka GA, Borg LE, Hutcheon ID, Sharp MA, Anbar AD (2010) Natural variations in uranium isotope ratios of uranium ore concentrates: Understanding the U-238/U-235 fractionation mechanism. *Earth Planet Sci Lett* 291(1–4):228–233.
4. Brennecka GA, Herrmann AD, Algeo TJ, Anbar AD (2011) Rapid expansion of oceanic anoxia immediately before the end-Permian mass extinction. *Proc Natl Acad Sci USA* 108(43):17631–17634.
5. Li L, Steefel CI, Williams KH, Wilkins MJ, Hubbard SS (2009) Mineral transformation and biomass accumulation associated with uranium bioremediation at Rifle, Colorado. *Environ Sci Technol* 43(14):5429–5435.
6. Yabusaki SB, et al. (2011) Variably saturated flow and multicomponent biogeochemical reactive transport modeling of a uranium bioremediation field experiment. *J Contam Hydrol* 126(3–4):271–290.
7. Alessi DS, et al. (2012) Quantitative separation of monomeric U(IV) from UO_2 in products of U(VI) reduction. *Environ Sci Technol* 46(11):6150–6157.
8. Sharp JO, et al. (2011) Uranium speciation and stability after reductive immobilization in aquifer sediments. *Geochim Cosmochim Acta* 75(21):6497–6510.
9. Bernier-Latmani R, et al. (2010) Non-uraninite products of microbial U(VI) reduction. *Environ Sci Technol* 44(24):9456–9462.
10. Ray AE, et al. (2011) Evidence for multiple modes of uranium immobilization by an anaerobic bacterium. *Geochim Cosmochim Acta* 75(10):2684–2695.
11. Fletcher KE, et al. (2010) U(VI) reduction to mononuclear U(IV) by *Desulfitobacterium* species. *Environ Sci Technol* 44(12):4705–4709.
12. Boyanov MI, et al. (2011) Solution and microbial controls on the formation of reduced U(IV) species. *Environ Sci Technol* 45(19):8336–8344.
13. Kelly SD, et al. (2010) Uranium transformations in static microcosms. *Environ Sci Technol* 44(1):236–242.
14. Sivaswamy V, et al. (2011) Multiple mechanisms of uranium immobilization by Cellulomonas sp. strain ES6. *Biotechnol Bioeng* 108(2):264–276.
15. Kelly SD, et al. (2008) Speciation of uranium in sediments before and after *in situ* biostimulation. *Environ Sci Technol* 42(5):1558–1564.

16. Campbell KM, et al. (2012) Geochemical, mineralogical and microbiological characteristics of sediment from a naturally reduced zone in a uranium-contaminated aquifer. *Appl Geochem* 27(8):1499–1511.
17. Reynolds RL, Goldhaber MB, Carpenter DJ (1982) Biogenic and nonbiogenic ore-forming processes in the south Texas uranium district: Evidence from the Panna Maria deposit. *Econ Geol* 77(3):541–556.
18. Min M, Chen J, Wang J, Wei G, Fayek M (2005) Mineral-hosted paragenesis and textures associated with sandstone-hosted roll-front uranium deposits, NW China. *Ore Geol Rev* 26(1–2):51–69.
19. Cai CF, et al. (2007) Mineralogical and geochemical evidence for coupled bacterial uranium mineralization and hydrocarbon oxidation in the Shashagetai deposit, NW China. *Chem Geol* 236(1–2):167–179.
20. Cai CF, et al. (2007) Biogenic and petroleum-related ore-forming processes in Dongsheng uranium deposit, NW China. *Ore Geol Rev* 32(1–2):262–274.
21. Jensen ML (1958) Sulfur isotopes and the origin of sandstone-type uranium deposits. *Econ Geol* 53:598–616.
22. Reynolds RL, Goldhaber MB (1983) Iron disfulfide minerals and the genesis of roll-type uranium deposits. *Econ Geol* 78(1):105–120.
23. Lovley DR, Phillips EJP (1992) Reduction of uranium by *Desulfovibrio desulfuricans*. *Appl Environ Microbiol* 58(3):850–856.
24. Lovley DR, Phillips EJP, Gorby YA, Landa ER (1991) Microbial reduction of uranium. *Nature* 350(6317):413–416.
25. Long PE, Yabusaki SB, Meyer PD, Murray CJ, N'Guessan AL (2008) *Technical Basis for Assessing Uranium Bioremediation Performance* (Office of Nuclear Regulatory Research, Washington, DC), NUREG Report NUREG/CR-6973, p 118.
26. Wilkins MJ, et al. (2011) Development of a biomarker for Geobacter activity and strain composition; proteogenomic analysis of the citrate synthase protein during bioremediation of U(VI). *Microb Biotechnol* 4(1):55–63.
27. Williams KH, et al. (2011) Acetate availability and its influence on sustainable bioremediation of uranium-contaminated groundwater. *Geomicrobiol J* 28(5–6): 519–539.
28. Chen Z, et al. (2012) Diversity of microbial community in Shihongtan sandstone-type uranium deposits, Xinjiang, China. *Geomicrobiol J* 29(3):255–263.
29. Wersin P, et al. (1994) Interaction between aqueous uranium and sulfide minerals—spectroscopic evidence for sorption and reduction. *Geochim Cosmochim Acta* 58(13): 2829–2843.
30. Descostes M, et al. (2010) Uptake of uranium and trace elements in pyrite (FeS_2) suspensions. *Geochim Cosmochim Acta* 74(5):1551–1562.
31. Hua B, Xu H, Terry J, Deng B (2006) Kinetics of uranium(VI) reduction by hydrogen sulfide in anoxic aqueous systems. *Environ Sci Technol* 40(15):4666–4671.
32. Scott TB, Tort OR, Allen GC (2007) Aqueous uptake of uranium onto pyrite surfaces; reactivity of fresh versus weathered material. *Geochim Cosmochim Acta* 71(21): 5044–5053.
33. Moyes LN, et al. (2000) Uranium uptake from aqueous solution by interaction with goethite, lepidocrocite, muscovite, and mackinawite: An X-ray absorption spectroscopy study. *Environ Sci Technol* 34(6):1062–1068.
34. Hyun SP, Davis JA, Sun K, Hayes KF (2012) Uranium(VI) reduction by iron(II) monosulfide mackinawite. *Environ Sci Technol* 46(6):3369–3376.
35. Latta DE, et al. (2012) Influence of magnetite stoichiometry on U(VI) reduction. *Environ Sci Technol* 46(2):778–786.
36. Singer DM, et al. (2012) Identification of simultaneous U(VI) sorption complexes and U(IV) nanoprecipitates on the magnetite (111) surface. *Environ Sci Technol* 46(7): 3811–3820.
37. Veeramani H, et al. (2011) Products of abiotic U(VI) reduction by biogenic magnetite and vivianite. *Geochim Cosmochim Acta* 75(9):2512–2528.
38. O'Loughlin EJ, Kelly SD, Cook RE, Csencsits R, Kemner KM (2003) Reduction of uranium(VI) by mixed iron(II)/iron(III) hydroxide (green rust): Formation of UO_2 nanoparticles. *Environ Sci Technol* 37(4):721–727.
39. Liger E, Charlet L, Van Cappellen P (1999) Surface catalysis of uranium(VI) reduction by iron(II). *Geochim Cosmochim Acta* 63(19–20):2939–2955.
40. Latta DE, Boyanov MI, Kemner KM, O'Loughlin EJ, Scherer MM (2012) Abiotic reduction of uranium by Fe(II) in soil. *Appl Geochem* 27(8):1512–1524.
41. Long PE (2010) *Microbiological, Geochemical and Hydrologic Processes Controlling Uranium Mobility: An Integrated Field Scale Subsurface Research Challenge Site at Rifle, Colorado. February 2009 to January 2010.* (Department of Energy Office of Science, Subsurface Biogeochemistry Research Program, Richland, WA), Annual Report, PNNL-19167.
42. Moon HS, et al. (2010) Microbial reduction of uranium under iron- and sulfate-reducing conditions: Effect of amended goethite on microbial community composition and dynamics. *Water Res* 44(14):4015–4028.
43. Rickard DT (1975) Kinetics and mechanisms of pyrite formation at low temperatures. *Am J Sci* 275(6):636–652.
44. Li L, Steefel CI, Kowalsky MB, Englert A, Hubbard SS (2010) Effects of physical and geochemical heterogeneities on mineral transformation and biomass accumulation during biostimulation experiments at Rifle, Colorado. *J Contam Hydrol* 112(1–4): 45–63.
45. Department of Energy (2012) *Legacy Management Geospatial Environmental Mapping System*. Available at http://gems.lm.doe.gov/imf/sites/gems_continental_us/jsp/launch.jsp. Accessed November 6, 2012.
46. Komlos J, Peacock A, Kukkadapu RK, Jaffé PR (2008) Long-term dynamics of uranium reduction/reoxidation under low sulfate conditions. *Geochim Cosmochim Acta* 72(15): 3603–3615.
47. Cao B, et al. (2011) Contribution of extracellular polymeric substances from Shewanella sp. HRCR-1 biofilms to U(VI) immobilization. *Environ Sci Technol* 45(13): 5483–5490.
48. Schoonen MAA (2004) Mechanisms of Sedimentary Pyrite Formation, *Geological Society of America Special Papers*, eds Amend JP, Edwards KJ, Lyons TW (The Geological Society of America, Boulder, CO), Vol 379, pp 117–134.
49. Konhauser KO (1997) Bacterial iron biomineralisation in nature. *FEMS Microbiol Rev* 20(3–4):315–326.
50. Druhan JL, et al. (2008) Sulfur isotopes as indicators of amended bacterial sulfate reduction processes influencing field scale uranium bioremediation. *Environ Sci Technol* 42(21):7842–7849.
51. Long PE (2011) *Microbiological, Geochemical and Hydrologic Processes Controlling Uranium Mobility: An Integrated Field Scale Subsurface Research Challenge Site at Rifle, Colorado. February 2010 to January 2011* (Department of Energy Office of Science, Subsurface Biogeochemistry Research Program, Richland, WA), Annual Report, PNNL-20200.
52. Madigan MT, Martinko JM, Dunlap PV, Clark DP (2010) *Brock Biology of Microorganisms* (Pearson/Benjamin Cummings, San Francisco), 13th Ed.
53. Bencheikh-Latmani R, Leckie JO (2003) Association of uranyl with the cell wall of Pseudomonas fluorescens inhibits metabolism. *Geochim Cosmochim Acta* 67(21): 4057–4066.
54. Gorby YA, Lovley DR (1992) Enzymatic uranium precipitation. *Environ Sci Technol* 26(1):205–207.
55. Bopp CJ, 4th, et al. (2010) Uranium $^{238}U/^{235}U$ isotope ratios as indicators of reduction: Results from an in situ biostimulation experiment at Rifle, Colorado, U.S.A. *Environ Sci Technol* 44(15):5927–5933.
56. Bopp CJ, Lundstrom CC, Johnson TM, Glessner JJG (2009) Variations in U-238/U-235 in uranium ore deposits: Isotopic signatures of the U reduction process? *Geology* 37(7): 611–614.
57. Abdelouas A, Lutze W, Nuttall HE (1999) Oxidative dissolution of uraninite precipitated on Navajo Sandstone. *J Contam Hydrol* 36(3–4):353–375.
58. Bi Y, Hyun SP, Kukkadapu RK, Hayes KF (2013) Oxidative dissolution of UO_2 in a simulated groundwater containing synthetic nanocrystalline mackinawite. *Geochim Cosmochim Acta* 102:175–190.
59. del Villar LP, et al. (2005) Hydrogeochemical evolution and C isotope study of groundwaters from "Mina Fe" U deposit (Salamanca, Spain): Implications for processes in radwaste disposal. *Appl Geochem* 20(3):465–485.
60. Landais P, Dubessy J, Poty B, Robb LJ (1990) 3 examples illustrating the analysis of organic matter associated with uranium ores. *Org Geochem* 16(1–3):601–608.
61. Verma MB, Dandele PS, Babu GN, Umamaheswar K, Maithani PB (2011) Hydro-uranium anomalies as an effective tool in exploration of concealed unconformity related U-deposit in Srisailam sub-basin, Andhra Pradesh—case study from Chitrial area. *J Geol Soc India* 78(5):468–476.
62. Yue SJ, Wang GC (2011) Relationship between the hydrogeochemical environment and sandstone-type uranium mineralization in the Ili basin, China. *Appl Geochem* 26(1):133–139.
63. Mossman DJ, Nagy B, Davis DW (1993) Hydrothermal alteration of organic-matter in uranium ores, Elliot Lake, Canada. Implications for selected organic-rich deposits. *Geochim Cosmochim Acta* 57(14):3251–3259.
64. Min MZ, et al. (2007) Hydrochemistry and isotope compositions of groundwater from the Shihongtan sandstone-hosted uranium deposit, Xinjiang, NW China. *J Geochem Explor* 93(2):91–108.
65. Salas J, Ayora C (2004) Groundwater chemistry of the Okélobondo uraninite deposit area (Oklo, Gabon): Two-dimensional reactive transport modelling. *J Contam Hydrol* 69(1–2):115–137.
66. Yanase N, Payne TE, Sekine K (1995) Groundwater geochemistry in the Koongarra ore deposit, Austrailia. 1. Implications for uranium migration. *Geochem J* 29(1):1–29.
67. Plant JA, Simpson PR, Smith B, Windley BF (1999) *Uranium Ore Deposits-Products of the Radioactive Earth. Uranium: Mineralogy, Geochemistry, and the Environment*, Reviews in Mineralogy (Mineralogical Society of America, Washington, DC), Vol 38, pp 255–319.
68. Doinikova OA (2007) Uranium deposits with a new phosphate type of blacks. *Geology of Ore Deposits* 49(1):80–86.
69. Hua B, Deng BL (2008) Reductive immobilization of uranium(VI) by amorphous iron sulfide. *Environ Sci Technol* 42(23):8703–8708.
70. Stadelmann P (2012) The Java Electron Microscopy Software (JEMS) (Interdisciplinary Centre for Electron Microscopy, Lausanne, Switzerland). Available at http://cimewww.epfl.ch/people/stadelmann/jemswebsite/jems.html.
71. Selenska S, Klingmüller W (1991) DNA recovery and direct detection of Tn5 sequences from soil. *Lett Appl Microbiol* 13(1):21–24.
72. Edgar RC (2010) Search and clustering orders of magnitude faster than BLAST. *Bioinformatics* 26(19):2460–2461.
73. Caporaso JG, et al. (2010) PyNAST: A flexible tool for aligning sequences to a template alignment. *Bioinformatics* 26(2):266–267.
74. Wang Q, Garrity GM, Tiedje JM, Cole JR (2007) Naive Bayesian classifier for rapid assignment of rRNA sequences into the new bacterial taxonomy. *Appl Environ Microbiol* 73(16):5261–5267.
75. Webb SM (2011) The MicroAnalysis Toolkit: X-ray fluorescence image processing software. *AIP Conf Proc* 1365:196–199.
76. Webb SM (2005) SIXpack: A graphical user interface for XAS analysis using IFEFFIT. *Phys Scr T* 115:1011–1014.
77. Ravel B, Newville M (2005) ATHENA, ARTEMIS, HEPHAESTUS: Data analysis for X-ray absorption spectroscopy using IFEFFIT. *J Synchrotron Radiat* 12(Pt 4):537–541.
78. Rehr JJ, Albers RC, Zabinsky SI (1992) High-order multiple-scattering calculations of x-ray-absorption fine structure. *Phys Rev Lett* 69(23):3397–3400.